[handwritten: text from]

3.4 Pion absorption from the lowest atomic orbital

[handwritten: → separate page]

3.4.1 Pion absorption in ^{2}H
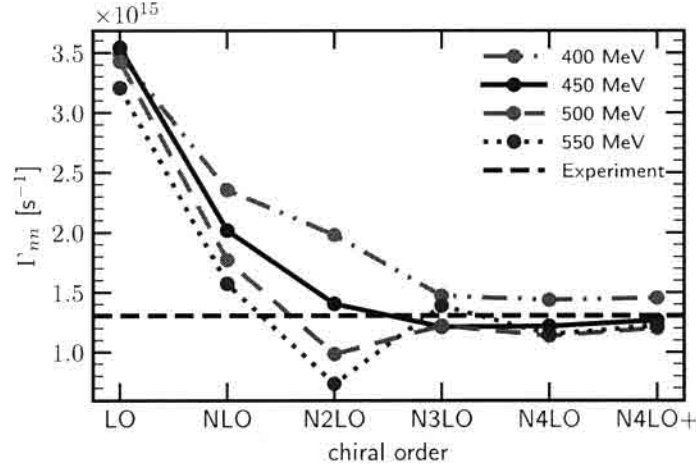

Figure 3.48: Absorption rate for the $\pi^- + {}^2\text{H} \to n+n$ reaction. The rates were calculated using the SMS force with different chiral orders and cut-off values. The results were obtained using the single-nucleon transition operator and supplemented by two-nucleon contributions at the leading order. The figure shows the results obtained using the plane wave (PW) plus two-neutron rescattering (Full) parts. The experimental value is extracted from the hadronic ground-state broadening in pionic deuterium and is taken from Refs. [81,85].

In Fig. 3.48 the absorption rate Γ_{nn} is shown for the process $\pi^- + {}^2\text{H} \to n + n$ as a function of the chiral order (horizontal axis) and the cutoff parameter (different lines) together with experimental data extracted from [81,85]. We see a significant difference between predictions obtained using different Λ. The impact of chiral orders is large at LO and NLO (each subsequent order differs from the previous by $\sim 40\,\%$ and $\sim 30\,\%$, respectively) and is gradually decreasing, and N^{3}LO-N^{4}LO-N^{4}LO$^+$ steps are almost invisible (the relative difference between subsequent orders is $\sim 5\,\%$). The comparison with experimental data shows that our predictions converge to a correct value coming closely to it all large chiral orders and Λs except $\Lambda = 450$ MeV which is clearly separated from other predictions. The bias $\Gamma_{nn}^{550} - \Gamma_{nn}^{exp}$ is still $0.178 \times 10^{15}\,\text{s}^{-1}$ which is $12.7\,\%$. Such a result reveals that NN interaction with $\Lambda = 450$ MeV is inadequate in data description. However, using it gives an additional measure of uncertainty related to the cut-off parameter value.

3.4.2 Pion absorption in ^{3}He

In Fig. 3.49 and 3.50 the total pion absorption rates are presented as a function of the chiral order and for different values of the cut-off parameter for $\pi^- + {}^3\text{He} \to p+n+n$ and $\pi^- + {}^3\text{He} \to n+d$ reactions, respectively. Both figures show that with fixed chiral order the arrangement of absorption rates obtained with various values of the cut-off parameter remains the same, namely with increasing Λ, the absorption rate decreases. The only exception in both cases appears at N^{3}LO where prediction with $\Lambda = 550$ MeV goes above

In the following subsections I present my results for the pion absorption processes on ^2H, ^3H, and ^3He. For these reactions the total absorption rate is an observable which attracts the most attention, mainly due to the relatively simple experiments needed to measure it. Namely, in such measurements only detection of nucleons is required but there is no need to measure their momenta or energies. In the case of the pion absorption on ^2H, if measurement is restricted to unpolarized particles, the capture rate is the only interesting observable. That is because the initial state is in rest what is a reason for opposite momenta of two neutrons in the final state. Due to the rotational symmetry directions of those momenta are not important. In contrast, in the case of absorption on 3N bound states one can be also interested in various differential absorption rates. Thus in following I show for apsorption on ^3He and ^3H prediction for the differential and total capture rates, while for the absorptio on the deuteron I will restrict myself to the latter one.

other predictions. At the next order, N⁴LO, it comes back to the usual arrangement. This behavior may be connected to the ³He wave function resulting from the 3NF used for the calculation. In order to prove that, I show in Fig. 3.51 a corresponding figure for a ³He proton radius r_p calculated with and without 3NF (left and right panels, respectively). Results obtained with the 3NF show similar deviation at N³LO while the radius computed without the 3NF does not. Nevertheless, the spread of predictions concerning the cut-off values seen in Fig. 3.51 is much smaller with the 3NF and deviation seems to be not crucial as the total difference between predictions in this case is very small.

There are also experimental data for the Γ_{pnn} and Γ_{nd} available on the market. As it was discussed in [86], experimental data for the Γ_{pnn} and Γ_{nd} can be extracted from [87–89] and it is *they are*

$$\Gamma_{pnn}^{\text{exp.}} = (2.47 \pm 0.65) \times 10^{16}\,\text{s}^{-1} \tag{3.3}$$
$$\Gamma_{nd}^{\text{exp.}} = (6.8 \pm 1.9) \times 10^{15}\,\text{s}^{-1}. \tag{3.4}$$

My predictions can be summarized as follows:

$$\Gamma_{pnn} = (1.28^{+0.29}_{-0.14} \pm 1.02) \times 10^{16}\,\text{s}^{-1} \tag{3.5}$$
$$\Gamma_{nd} = (2.0^{+1.0}_{-0.6} \pm 1.6) \times 10^{15}\,\text{s}^{-1} \tag{3.6}$$
$$\tag{3.7}$$

where the first error is related to the cut-off parameter and the second one to the chiral order (truncation error). We see that our predictions, presented in Figs. 3.49 and 3.50, are smaller than experimental values, but they overlap each other within the uncertainty range, giving large experimental errors as well as theoretical ones.
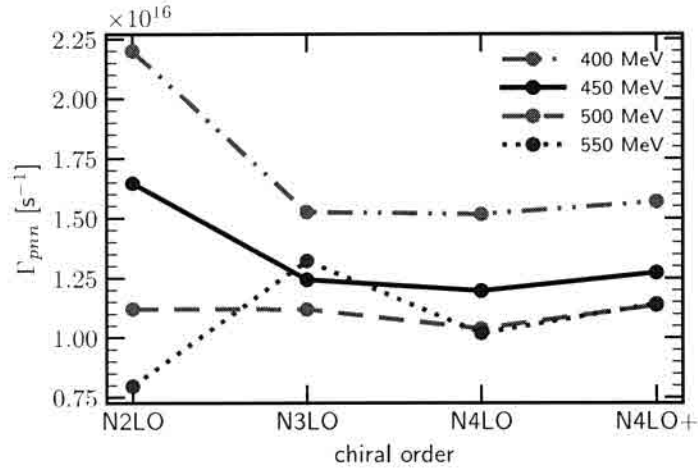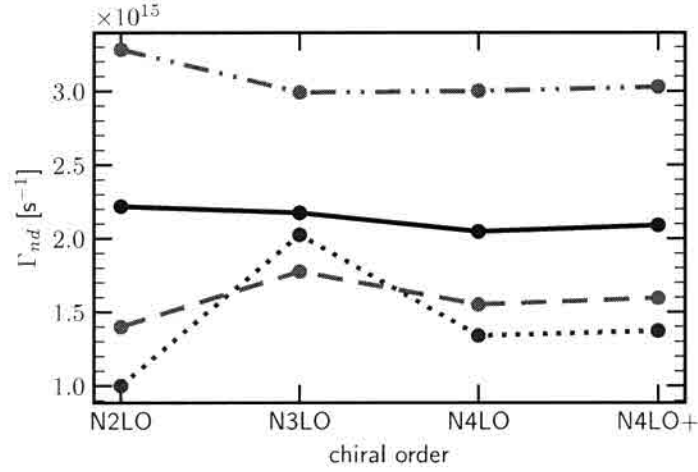

Figure 3.49: Absorption rate for $\pi^- + {}^3\text{He} \to p + n + n$ reaction as a function of the chiral order and with different values of the cut-off parameter Λ. Predictions were obtained with the SMS NN interaction at a given order combined with N²LO 3NF.

By its nature, the total absorption rates cannot deliver details on the distribution of

Figure 3.50: The same as in Fig. 3.49, but for $\pi^- +^3 \text{He} \to n + d$ reaction.
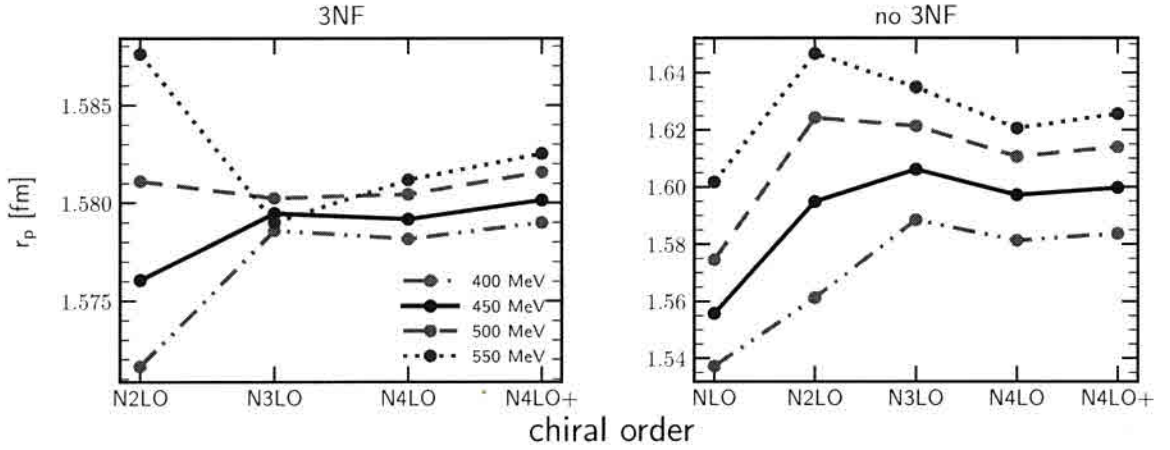
Figure 3.51: *check ml3* Proton radius r_p as a function of the chiral order calculated with different values of the cut-off parameter Λ. The radius was calculated with 2NF and 3NF (left panel) or with 2NF only (right panel).

contributions arising from various dynamical ingredients to the absorption process in the phase space. Thus in the following, I show various intensity plots revealing phase-space regions of special interest.

Let me remind that in the case of absorption rates, only two kinetical variables are necessary to define the exclusive kinematical configuration. That is, because for that process there is full rotational symmetry, as none of the vectors define the $(\hat{z})$-axis.

In Figs. 3.52 and 3.53 I show such intensity plots for the double differential absorption rates $d^2\Gamma_{pnn}/dE_1 dE_2$ for the $\pi^- +^3 \text{He} \to p + n + n$ process as functions of the nucleons energies (assuming nucleon number 1 to be a proton) and of the Dalitz coordinates (x and y), respectively.

The coordinates x and y are defined as:

Table 3.1: Absorption rates in the four regions of the phase space I_i defined in Ref. [58] for the $\pi^- + {}^3\text{He} \to p + n + n$ reaction calculated with the chiral SMS NN potential supplemented by 3NF at N^{2}LO with different values of the cutoff parameter Λ.

Λ (MeV)	Normalized absorption rates Γ_i			
	I_1	I_2	I_3	I_4
400	0.804	0.152	0.029	0.016
450	0.797	0.152	0.032	0.019
500	0.792	0.152	0.035	0.021
550	0.793	0.151	0.036	0.020
Gotta et al. [58]	0.844	0.099	0.033	0.023

[handwritten: add infos where QFS geometry from our paper to in (x,y) variables. Take this]

$$x = 3(E_1 + 2E_2 - E)/E,$$
$$y = (3E_1 - E)/E,$$
(3.8)

where E is a total kinetic 3N energy. These coordinates are restricted to the region where $r^2 \equiv x^2 + y^2 \leq 1$.

Each of the two figures consists of four panels representing predictions obtained with different values of the cut-off parameter Λ. The difference between predictions which can be immediately noticed with the naked eye is that the area of the central region (corresponding to the smallest rates) becomes larger with increasing Λ. It coheres to what we saw in Fig. 3.49 where the total absorption rate was inversely correlated with the cut-off parameter. The dominant contribution comes from the region with the lowest proton energy values of $E_1 \to 0$ where both neutron energies have similar large values. This is a situation of quasi-free scattering(QFS) - when a proton is a spectator and both neutrons share equally all energy.

[handwritten left margin: reasonable]

Another region with a high absorption rate is the neutron-neutron final state interaction configuration (FSI(nn)). It is located at high E_1 values when a proton gets two-thirds part of the total energy while neutrons both get one-sixth. In Fig. 3.52 we see this region at the very right region (with $E_1 \to 85$) with rapid growth of the absorption rate and it is observed at every value of the cut-off parameter. The very same region is presented in Fig. 3.55 at $y \to 1$. *Explain what happens with the rest of energy?*

[handwritten left margin: or, or, $i=1,...,4$]

In [86] we have shown the comparison of our predictions with one more experimental data, from [58]. In that paper, the authors consider four specific regions (I_i for $i = 1, 2, 3, 4$) and give experimental results for each of them separately. The renormalization procedure was applied to our predictions in order to compare results with experimental data. Following [58], we divide the predictions for each particular region (Γ_i) by the total value $\sum_{i=1}^{4} \Gamma_i$. Results are presented in the Table 3.1.

We see that our predictions are very close to experimental results and retrieve the same pattern of the absorption rate distribution over the regarded regions. *

Next in Figs. 3.54 and 3.55 I show similar intensity plots for the predictions obtained with plane wave component only (without rescattering part). They reveal that the difference of predictions obtained without rescattering part with ones including it (Figs. 3.52 and 3.53) is very large. Predicted values are a few times larger and the distribution of dominant areas is completely different. The FSI(nn) region is not presented here in the sense that there is no peak concerning other regions. That is natural, as the FSI(nn)

[handwritten left margin: big]

[handwritten: compared to ?]

*[handwritten bottom: * The observed discrepancy can arise from the higher contribution to the nuclear current, what should be checked in the future.]*
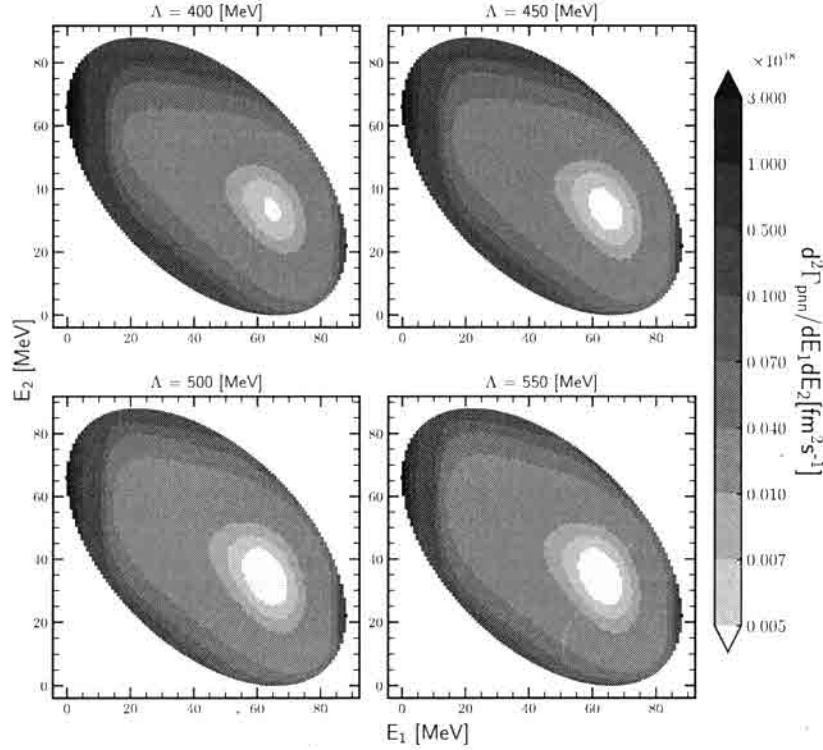
Figure 3.52: Intensity plots for the double differential absorption rates $d^2\Gamma_{pnn}/dE_1dE_2$ for the $\pi^- +\ ^3\mathrm{He} \rightarrow p + n + n$ process, obtained using the SMS NN potential with all contributions possible: plane wave + rescattering, 1NC + 2N, 2NF–3NF. Each panel presents predictions obtained with different values of the cut-off parameter Λ: from $\Lambda = 400\,\mathrm{MeV}$ (upper left) to $\Lambda = 550\,\mathrm{MeV}$ (lower right). Nucleon 1 is a proton.

peak arises from strong interaction in the final state, which by definition is not in the plane wave approximation. On the contrary, the QFS region is presented. Results of Figs. 3.54 and 3.55 tell us that one has to take into account the rescattering part in order to obtain realistic predictions for that process.

Results have been obtained with plane wave plus rescattering parts but with the single nucleon current only are presented in Figs. 3.56 and 3.57. As previously, each panel in the figures presents predictions obtained with different values of the cut-off parameter Λ. In contrast to the combinations shown above, the change in the cut-off value has a larger impact here: we observe that there is a different pattern in each panel. It does not change dramatically, but two peaks inside the figure become more or less clear. On the other hand, the distribution of the absorption rate is very different from the one, obtained with a more complete components setup (Figs. 3.52 and 3.53).

Figs. 3.58 and 3.59 show predictions obtained using similar dynamical components as in Figs. 3.52 and 3.53, but each panel includes predictions obtained with different chiral orders of the SMS potential. We see that predictions are not sensitive to the chiral order and even N^{2}LO predictions are pretty much similar to ones obtained with the most advanced N^{4}LO potential.

Presented above intensity plots correspond to exclusive processes with two particles detected. Now we would like to test if the same behavior of the capture rate is observed for the semi-inclusive observables. Thus following figures demonstrate the same phenomena
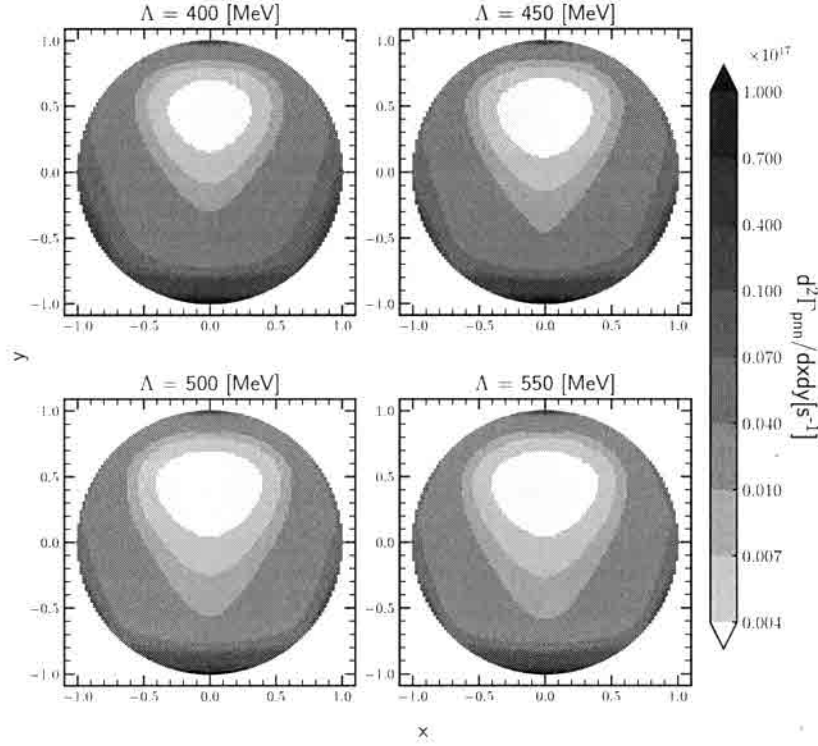
Figure 3.53: The same as in Fig. 3.52 but for the double differential absorption rates $d^2\Gamma_{pnn}/dxdy$.

but from a different point of view. Namely in Fig. 3.60 I show differential absorption rate $d\Gamma_{pnn}/dE_p$ that is the same as in e.g. Fig. 3.58, but integrated over E_n. All the results are obtained with the most advanced setup (plane wave – rescattering, 1NC – 2N, 2NF+3NF). The left panel consists of the results with $\Lambda = 450\,\text{MeV}$ and each curve corresponds to a particular chiral order. An interesting region here is a maximum of $d\Gamma_{pnn}/dE_p$ which corresponds to the bottom part of the circles from Fig. 3.58. At the point of maximum N²LO prediction distinguishes from other results as its ~~point of~~ maximum is noticeably higher. At $E_p = 0.92\,\text{MeV}$ (maximum point) the value of N²LO is 1.37 times larger than one from N⁴LO⁺ $(3.44 \times 10^{17}\,\text{fm}\,\text{s}^{-1}$ vs $2.52 \times 10^{17}\,\text{fm}\,\text{s}^{-1})$ the relative difference is 31.1 %. At the same time, the relative difference between all the predictions except for N²LO is 8.3 %.

The right panel of the Fig. 3.60 shows a cut-off dependence of the ~~predictions~~ obtained with the SMS NN chiral potential at N⁴LO⁺ supplemented by N²LO 3NF. In this case, the maximum point is interesting as well. We see that predictions with $\Lambda = 500\,\text{MeV}$ and $550\,\text{MeV}$ are quite close to each other: the relative difference between them at $E_p = 0.92\,\text{MeV}$ is only 1.5 %. In turn the spread between $\Lambda = 400\,\text{MeV}$, $450\,\text{MeV}$ and $500\,\text{MeV}$ is 40 % (at the same E_p). This cut-off dependence is hidden when looking at the colormaps Fig. 3.52, but from this perspective it is clearly presented. Anyway, the highest Λ, the biggest $d\Gamma_{pnn}/dE_p$ is ~~seen~~. That observable could be an ~~intensity~~ test for the cut-off value, however, it requires measurement at low proton energy ($\sim 0.8 - 1.0\,\text{MeV}$) which is an experimental challenge.

Similarly in Fig. 3.61 $d\Gamma_{pnn}/dE_n$ is presented. We observe similar trends as above. They are also shown up at the maximum point, which is around $E_n = 66.9\,\text{MeV}$ now:
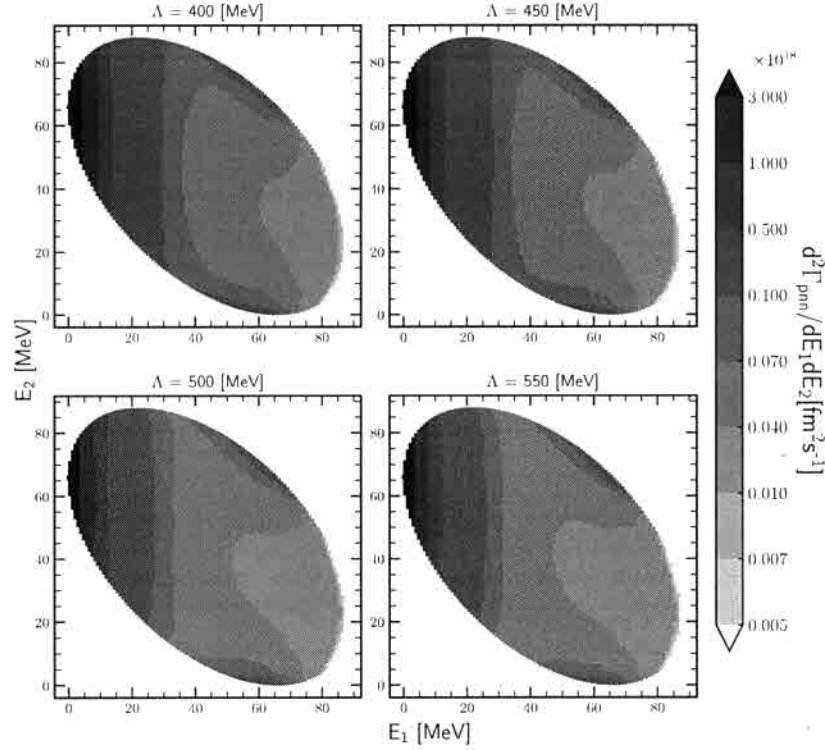
Figure 3.54: Intensity plots for the double differential absorption rates $d^2\Gamma_{pnn}/dE_1dE_2$ for the $\pi^- +^3$ He $\to p + n + n$ process obtained using the SMS NN potential at N^{4}LO$^+$ supplemented by N^{2}LO 3NF with plane wave part only (without rescattering). All other contributions are the same as in Fig. 3.52: 1NC + 2N and 2NF+3NF. Each panel presents predictions obtained with different values of the cut-off parameter Λ: from $\Lambda = 400$ MeV (upper left) to $\Lambda = 550$ MeV (lower right). Nucleon 1 is a proton.

the difference between N^{2}LO and N^{4}LO$^+$ predictions at this point is 29.0 %; the relative difference between all the predictions except for N^{2}LO is much smaller, but still is approx. 7.5 %; the N^{4}LO$^+$ predictions are also very similar for $\Lambda = 500$ MeV and 550 MeV (the spread is 1.6 %) while all remaining predictions are quite distinguished - the spread is 39.1 %. I find that observable very interesting in the context of experimental studies as a measurement of neutron at $E \approx 70$ MeV is nowadays within our reach.

Moving to the next figures, Fig. 3.62 and Fig. 3.63, I show 1-dim dependence of the absorption rate on the Dalitz coordinates $r = \sqrt{x^2 + y^2}$ and $\phi = \arctan \frac{y}{x}$, respectively. A similar trend is preserved, namely chiral order figures show that N^{2}LO predictions outstand from all other predictions, and noticeable cut-off dependence is observed.

In general, we can conclude that predictions are converged starting from the N^{3}LO chiral order (for NN force) as most of the demonstrated results show that the difference between N^{3}LO, N^{4}LO and N^{4}LO$^+$ is negligible. At the same time, we observe a strong cut-off dependence with predictions obtained with $\Lambda = 500$ MeV and 550 MeV being very similar, but with a large spread of all the rest results. This nature of the cut-off dependence is also reflected in the total absorption rate, presented in Fig. 3.49.
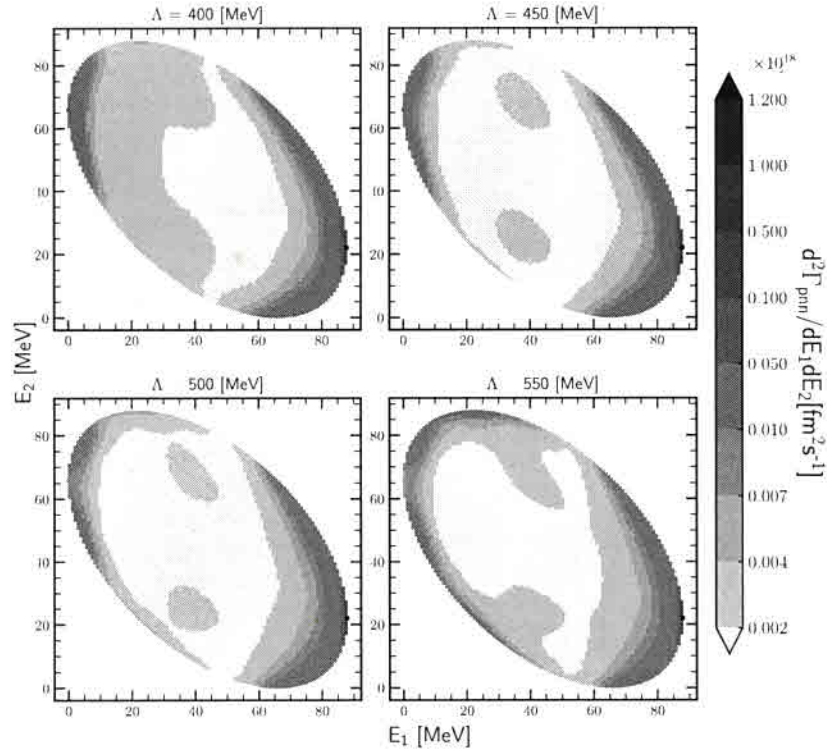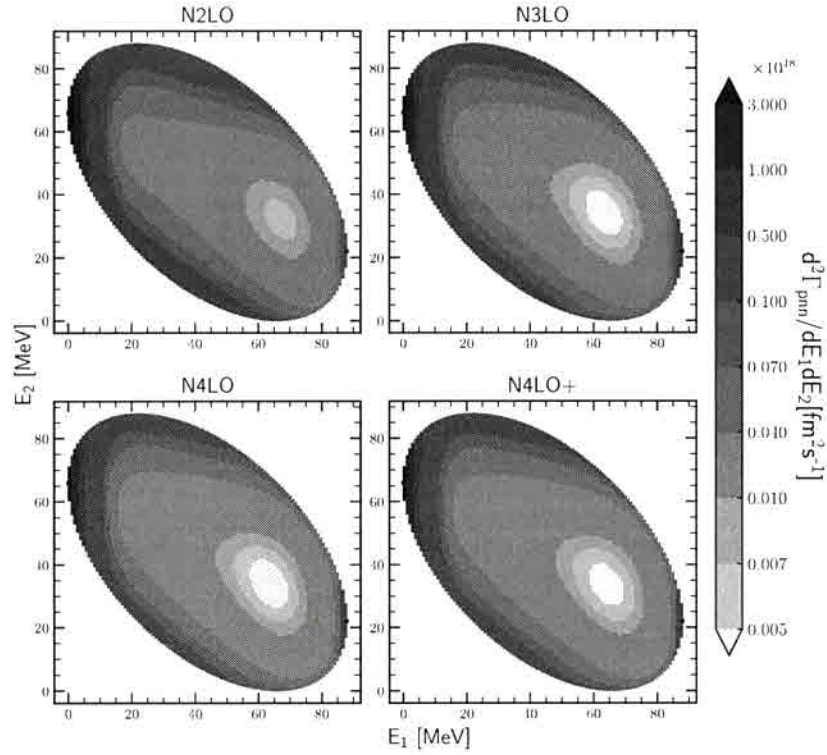
Figure 3.56: Intensity plots for the double differential absorption rates $d^2\Gamma_{pnn}/dE_1dE_2$ for the $\pi^- +^3$ He $\rightarrow p + n + n$ process obtained using the SMS NN potential at N^{4}LO$^+$ supplemented by N^{2}LO 3NF with 1NC only (without 2N) currents. All other contributions are the same as in Fig. 3.52: PWIAS+RESC and 2NF+3NF. Each panel presents predictions obtained with different values of the cut-off parameter Λ: from $\Lambda = 400$ MeV (upper left) to $\Lambda = 550$ MeV (lower right). Nucleon 1 is a proton.

Figure 3.58: Intensity plots for the double differential absorption rates $d^2\Gamma_{pnn}/dE_1dE_2$ for the $\pi^- + {}^3\text{He} \to p + n + n$ process obtained using the SMS potential at N⁴LO⁺ with all contributions possible: plane wave + rescattering, 1NC + 2N, 2NF+3NF. Each panel presents predictions obtained with different chiral orders of the SMS NN potential: from $N^2\text{LO}$ (upper left) to $N^4\text{LO}^+$ (lower right) and with $\Lambda = 450\,\text{MeV}$. Nucleon 1 is a proton. 3NF was taken at $N^2\text{LO}$ in each case.
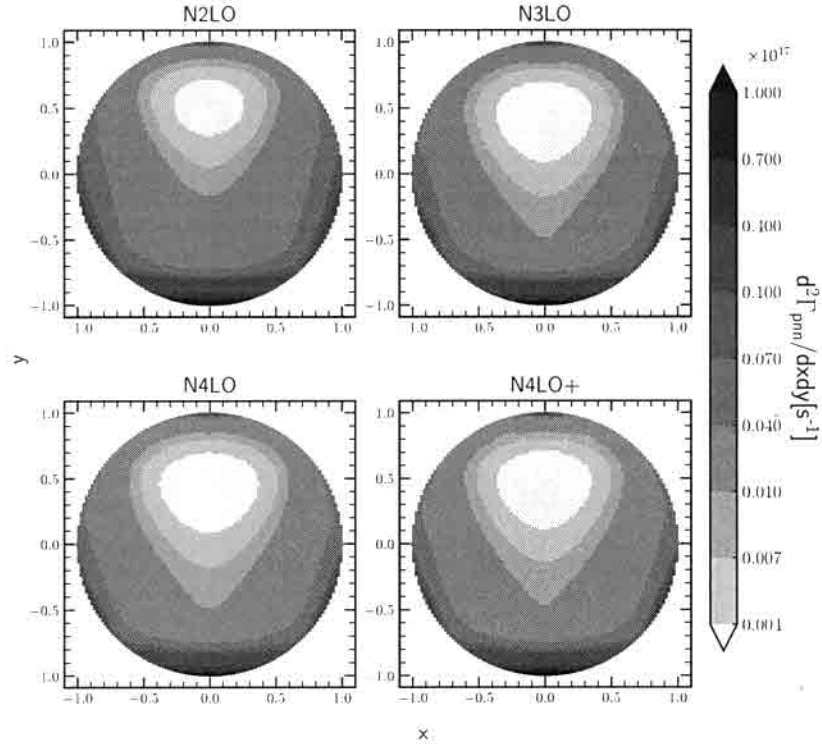
Figure 3.59: The same as in Fig. 3.58 but for the double differential absorption rates $d^2\Gamma_{pnn}/dxdy$.
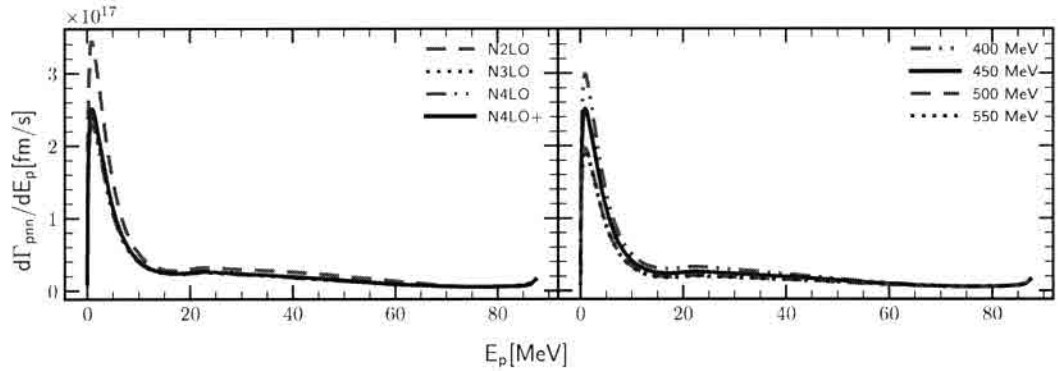

Figure 3.60: Differential absorption rate $d\Gamma_{pnn}/dE_p$ as a function of the proton energy E_p for the $\pi^- + {}^3\text{He} \rightarrow p+n+n$ process. Left panel shows results obtained with the NN N^{2}LO (green dashed line), N^{3}LO (blue dotted line), N^{4}LO (red dashed-double-dotted line) and N^{4}LO$^+$ (black solid line) chiral orders plus N^{2}LO 3NF, and with $\Lambda = 450$ MeV. The right panel includes results obtained with the N^{4}LO$^+$ SMS NN potential plus N^{2}LO 3NF with different values of the Λ: 400 MeV (red dashed-double-dotted line), Λ: 450 MeV (black solid line), Λ: 500 MeV (green dashed line line) and Λ: 550 MeV (blue dotted line). All predictions were obtained with "FULL-(1NC−2N)-(2NF+3NF)" setup.

3.4.3 Pion absorption in ^{3}H

In this subsection, I will show the results of calculations for the $\pi^- + {}^3\text{H} \to n + n + n$ process. In this case, only a three-body breakup is allowed as no two-body configuration can be composed out of three neutrons.

The total absorption rate Γ_{nnn} for that process is shown in Fig. 3.64 as a function of the chiral order of the SMS NN potential while each curve represents different cut-off values used to obtain the prediction. The most advanced dynamical model was used in this case, namely plane wave plus rescattering part, both single- and two-nucleon currents and two-nucleon plus three-nucleon interaction.

Similarly to the three-body break-up of ^{3}He, we see that with each subsequent chiral order predictions become closer to each other, so the cut-off dependence gets weaker. Also, the prediction with $\Lambda = 550\,\text{MeV}$ at N^{3}LO is strangely above the prediction with $\Lambda = 500\,\text{MeV}$. We can also notice, that at N^{4}LO predictions with cut-off values $500\,\text{MeV}$ and $550\,\text{MeV}$ are much closer to each other than to results obtained with other Λs.
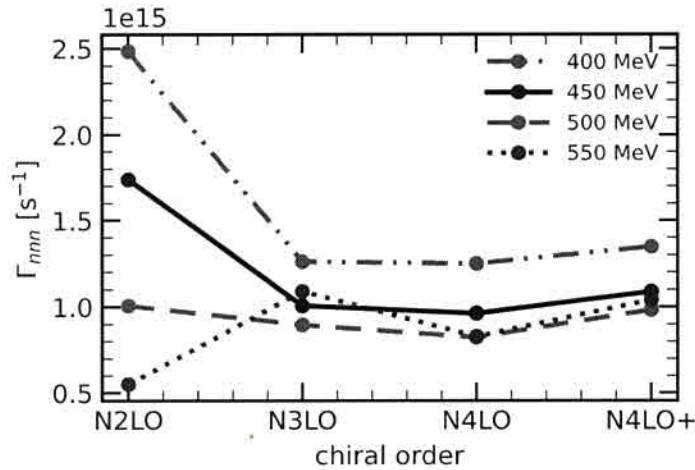

Figure 3.64: Absorption rate for $\pi^- + {}^3\text{H} \to n + n + n$ reaction as a function of the chiral order with different values of the cut-off parameter Λ. Predictions were obtained with 3NF at N^{2}LO.

In Figs. 3.65 and 3.66 I show intensity plots for the double differential absorption rates $d^2\Gamma_{nnn}/dE_1 dE_2$ for the $\pi^- + {}^3\text{H} \to n + n + n$ process as functions of the nucleons energies (Fig. 3.65) and of the Dalitz coordinates (Fig. 3.66), respectively. Each panel in the figures presents predictions obtained with different values of the cut-off parameter Λ. On the contrary to the ^{3}He case, we see a symmetric distribution of the absorption rate with respect to the center of the figure. It is because of the symmetry of the three-body system as we have three identical particles - neutrons. The dominant contribution comes from QFS(nn) regions - where one of the neutrons is a spectator and has the lowest energy (close to 0) and the rest two are sharing almost all the energy equally. In Fig. 3.65 these regions are around $(E_1, E_2) = (0, 65), (65, 0)$ and $(65, 65)$ MeV. Same regions are presented in Fig. 3.66 at around $(x, y) = (0, -1), (-0.85, 0.5)$ and $(0.85, 0.5)$. We see that predictions are not sensitive to the cut-off value. The only difference that can be noticed is in the distribution of the region with the lowest values of the Γ_{nnn} (the center of each figure). It is mostly probably caused by the fact that the very small values introduce larger calculational uncertainties.

Figs. 3.67 and 3.68 show similar intensity plots but each panel includes predictions obtained with different chiral orders of the SMS NN potential. Each of the panels shows very similar distributions of the absorption rate, except for the N²LO one, where the central region (with lowest Γ_{nnn} values) is less pronounced.

It is further confirmed by the Fig. 3.69 (left panel) where differential absorption rate $d\Gamma_{nnn}/dE_n$ at N²LO has much larger peaks (at around $E_n = 0\,\text{MeV}$ and $E_n = 68\,\text{MeV}$) while all the rest predictions are relatively close to each other. On the right panel of Fig. 3.69 we see that only the prediction obtained with $\Lambda = 400\,\text{MeV}$ is different from the rest. It is interesting to notice, as such a difference could not be observed from the colormaps.

Very similar tendency is observed in Figs. 3.70 and 3.71. In these figures I show differential absorption rate with respect to the Dalitz radial coordinates r and ϕ, respectively. The same as in Fig. 3.69 we see that N²LO and $\Lambda = 400\,\text{MeV}$ predictions are different from the rest, while all the other predictions are very close to each other.

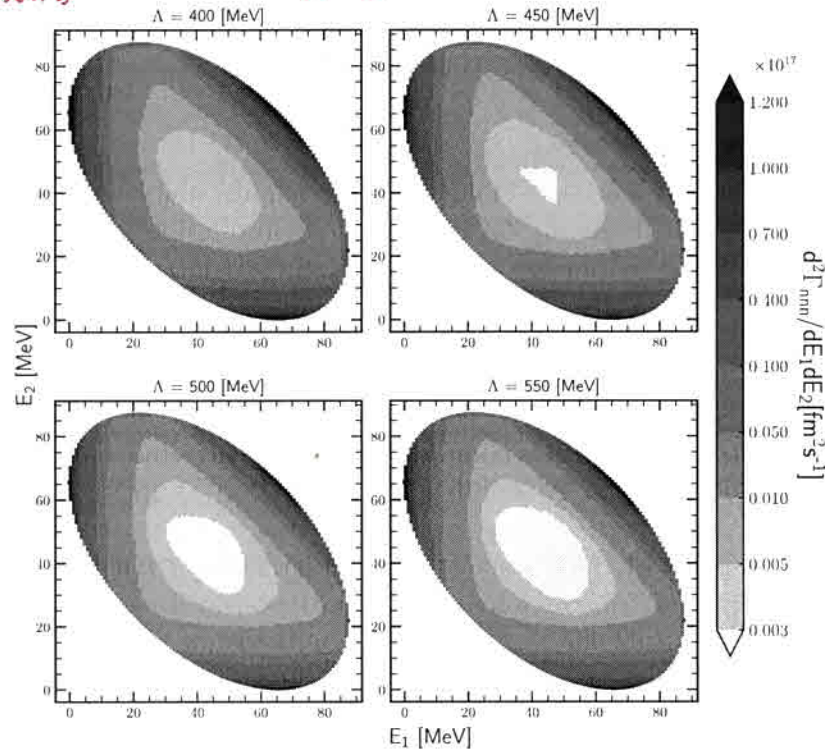Figure 3.65: Intensity plots for the double differential absorption rates $d^2\Gamma_{nnn}/dE_1 dE_2$ for the $\pi^- + {}^3\text{H} \to n + n + n$ process obtained using the SMS NN potential at N⁴LO⁺ supplemented by N²LO 3NF with all ingredients possible: plane wave + rescattering, 1NC + 2N, 2NF+3NF. Each panel presents predictions obtained with different values of the cut-off parameter Λ: from $400\,\text{MeV}$ (upper left) to $550\,\text{MeV}$ (lower right).
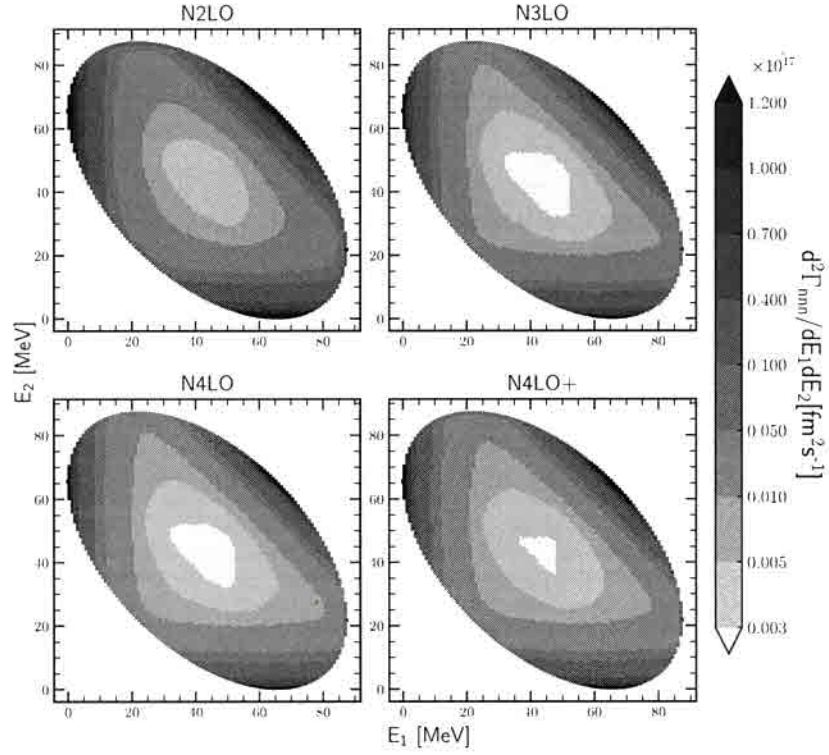
Figure 3.67: Intensity plots for the double differential absorption rates $d^2\Gamma_{nnn}/dE_1dE_2$ for the $\pi^- + {}^3\text{H} \to n + n + n$ process obtained using the SMS potential ~~at N4LO~~+ with all contributions possible: plane wave + rescattering, 1NC + 2N, 2NF+3NF. Each panel presents predictions obtained ~~with~~ different chiral orders of the SMS potential: from N^{2}LO (upper left) to N^{4}LO$^+$ (lower right) and with $\Lambda = 450\,\text{MeV}$. The 3NF is taken at N²LO in each case.
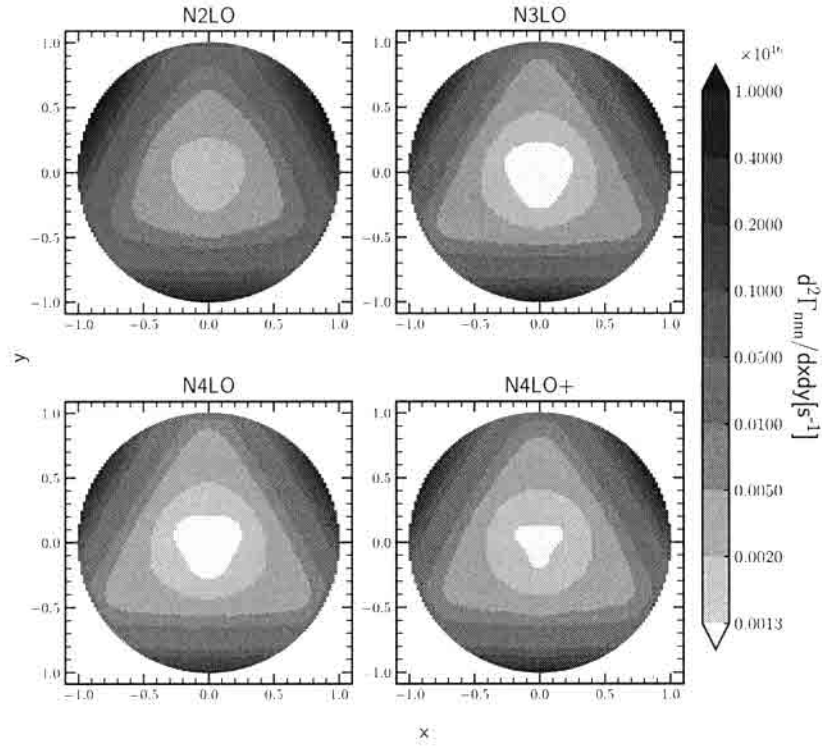
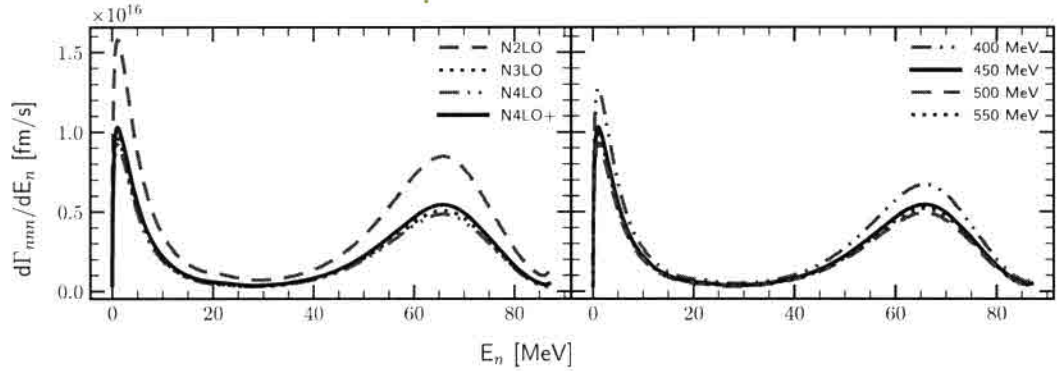Figure 3.68: The same as in Fig. 3.67 but for the double differential absorption rates $d^2\Gamma_{nnn}/dxdy$.

Figure 3.69: Differential absorption rate $d\Gamma_{nnn}/dE_n$ as a function of the neutron energy E_n for the $\pi^- + 3H \rightarrow n + n + n$ process. Left panel shows results obtained with NN force at glsn2lo (green dashed line), N^{3}LO (blue dotted line), N^{4}LO (red dashed-double-dotted line) and N^{4}LO$^+$ (black solid line) chiral orders, and with $\Lambda = 450\,$MeV. The N^{2}LO 3NF was used. The right panel includes results obtained with the N^{4}LO$^+$ NN SMS potential supplemented by the N^{2}LO 3NF with different values of the Λ: 400 MeV (red dashed-double-dotted line), Λ: 450 MeV (black solid line), Λ: 500 MeV (green dashed line line) and Λ: 550 MeV (blue dotted line). All predictions were obtained with "FULL-(1NC+2N)-(2NF+3NF)" setup.

also

plue wave + rescattering

maybe remove "FULL" from the thesis